Supplementary Information

Aggregation dynamics of nanoparticles at solid-liquid interfaces

Xuezeng Tian,[1,2] Haimei Zheng,[2,3,4] and Utkur Mirsaidov[1,5,6,7*]

1. Centre for BioImaging Sciences, Department of Biological Sciences, National University of Singapore, 117557, Singapore
2. Berkeley Education Alliance for Research in Singapore, 138602, Singapore
3. Materials Sciences Division, Lawrence Berkeley National Laboratory, Berkeley, CA 94720, USA
4. Department of Materials Science and Engineering, University of California, Berkeley, CA 94720, USA
5. Department of Physics, National University of Singapore, 117551, Singapore
6. NUSNNI-NanoCore, National University of Singapore, 117411, Singapore
7. Centre for Advanced 2D Materials, National University of Singapore, 117546, Singapore

[*]Correspondence: mirsaidov@nus.edu.sg

Table of Contents:

1. Image Analysis

Our image segmentation algorithm was implemented in the Miniconda Python software package[1] using the following libraries: numpy,[2] scipy,[3] opencv,[4] scikit-image,[5] cython,[6] mahotas,[7] and matplotlib.[8] We developed and implemented Python[1] codes for the image processing, which we described elsewhere.[9] The aggregation dynamics was extracted via segmentation and template matching of the individual NPs and aggregates in the recorded image sequences.

Segmentation. First, we inverted the raw image sequence frames and then performed background subtraction. Next, we applied a median filter of $\sigma = 5$ pixels to remove the high-frequency noise. Then, we obtained binary images using the Yen intensity thresholding algorithm.[1] At this stage, we represented the NPs and aggregates and background as 1 and 0, respectively, in the segmented binary images. Figure S1A shows the segmentation results corresponding to Figure 1B in the main text. Based on the segmented binary images, the number, size and movement of the aggregates were quantified for all the image frames.

Template matching for tracking translation and rotation. To quantify the translational and rotational movement of the aggregates, we applied a template matching algorithm with opencv[4] to the segmented binary images. To do this, we first selected an aggregate of interest to be the template. Next, we used an iterative approach to find the position and orientation of the aggregate in the other image frames. First, we located the same aggregate by finding the minimum of the averaged difference (i.e., error factor) between the template and the segmented aggregate.[10] Second, the template was rotated around its centre by 1°, and the first step of the template matching was applied again. By repeating the two steps above, the rotation angle was defined as the minimum of the error factors for the 360 template matching results. An example of the template matching results is shown in Figure S1B, and it corresponds to an aggregate in Figure 3D in the main text. The first white box includes the chosen template, and the subsequent boxes include the template-matched segmented aggregate.

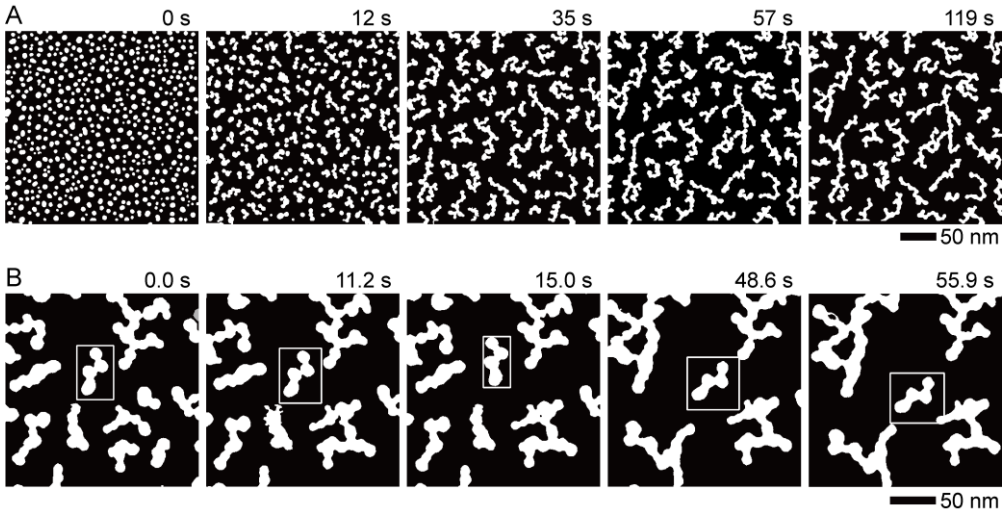

Figure S1. Examples of the processed TEM image time series. (**A**) Segmented binary image series of the aggregation process. (**B**) The template matching algorithm was used to track the translation and rotation of the boxed aggregate.

2. Box-counting method for estimating the fractal dimensions

In aggregates, the fractal dimension (D_f) is closely related to the aggregation kinetics and is an indicator of their packing density.[11] A small D_f indicates loose packing in an aggregate, whereas a large D_f corresponds to a compact aggregate.[12] To find the fractal dimensions of the aggregates, we used the box-counting algorithm.[9] We separated and covered an individual aggregate with a square box with a side length of r_{box}, and we counted the number of boxes, N_{box}, that covered the segmented aggregate. Next, to accurately capture the structure of the aggregate, we repeated this process with smaller boxes by gradually shrinking the box size down to 2 pixels in width. The fractal dimension, D_f, is defined as the slope of the log-log plot of N_{box} versus r_{box}.

$$D_f = {\log N_{box}}/{\log r_{box}} \quad (1)$$

3. Aggregation theory

The number of aggregates as a function of time, $N(t)$, during 2D aggregation is given by:[12]

$$N(t) \sim tln(t)^{-z} \quad (2)$$

where z is the kinetic exponent expressed through the diffusion coefficient of the aggregating particles as follows:

$$z = \frac{1}{1+\frac{2-d-\gamma D_f}{D_f}} \quad (3)$$

Here, d is the dimensionality of the system (in our case where the NPs diffuse on the membrane surface $d = 2$), D_f is the fractal dimension of the aggregates, and γ is the exponent of the diffusion coefficient (D), which is related to the aggregate size (S) by a power law: $D \sim S^{\gamma}$. For Brownian motion, $\gamma = 2$.

In our system, where the NPs diffuse and aggregate on the membrane surface ($d = 2$), we obtained

$$\gamma = 1 - \frac{1}{z} \quad (4)$$

4. More examples of aggregation kinetics in a thin water film

To study the influences of the different imaging conditions on the aggregation kinetics, we recorded more than 30 NP aggregation movies. The two additional examples shown in Figure S2A-B feature aggregation kinetics similar to the example in Figure 1. However, in Figure S2A-B, the aggregation process is faster compared to the aggregation in Figure 1. The difference in the aggregation rate is most likely due to a difference in the interaction strength between the NPs and the membrane in different liquid cells and/or the thickness of the water layer on the membrane in the liquid cells. To validate the trend observed in Figure 1D-E, we analysed ten more aggregation events imaged at the same magnification under the same electron flux in liquid cells with a comparable water layer thickness (estimated). Figure S2C and S2D show the average of the results. The relatively large error bars indicate that our measurements were sensitive to the liquid thickness, which cannot be easily controlled during the experiments. Nevertheless, the averaged aggregation kinetics results showed a fast initial aggregation and a gradual slowing of the kinetics at a later stage, which was consistent with our analysis in the main text (Figure 1D-E).

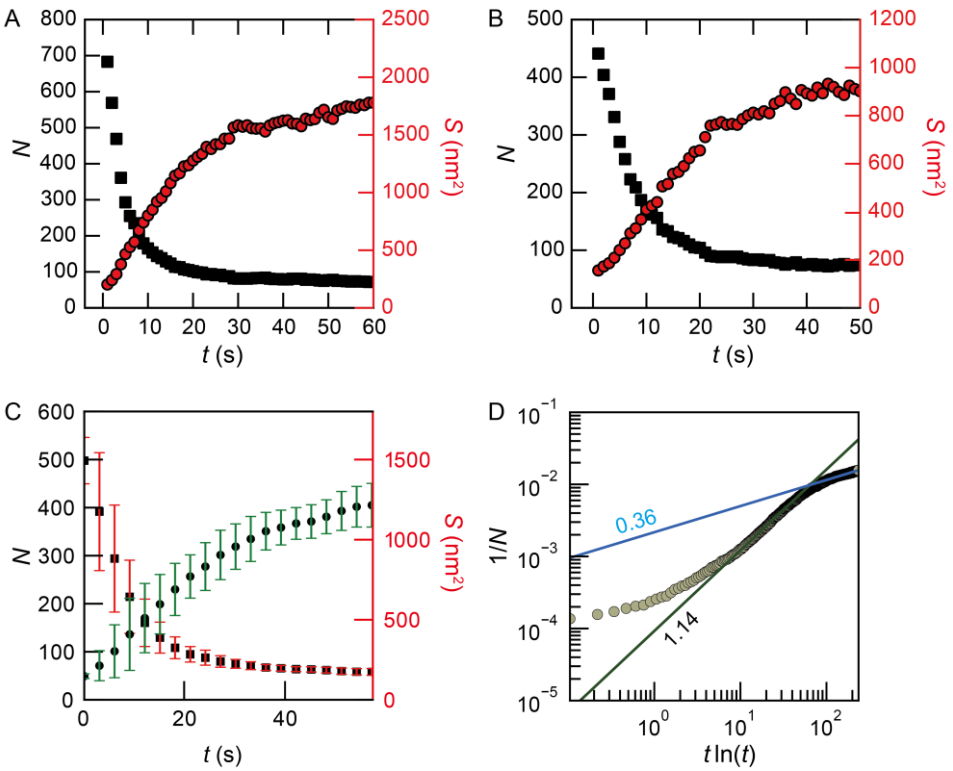

Figure S2. More examples of aggregation processes. Examples showing (**A**) the evolution of the average aggregate size (S) and (**B**) the aggregate number (N) as a function of time (t). (**C**) Evolution of the average number and size of the aggregates obtained from ten different movies. Error bars represent one standard deviation from the mean. (**D**) The log-log plot of the inverse aggregate number $(1/N)$ versus $t \ln t$ for the same ten movies. Here, the aggregation kinetic exponents are $z = 1.14$ and $z = 0.36$ for the early and late aggregation stages, respectively.

5. The influence of the liquid flow on aggregation

In our studies, we found that only the NPs and their aggregates in a region of the membrane with a thin ($\lesssim 20$ nm) water layer exhibited strong surface pinning, which was consistent with our previous studies that showed a suppressed mobility in thinner water layers.[13, 14] The bulk water between the top and bottom membranes was expelled from the field of view by the electron beam.[13, 15] The aggregation process is also influenced by the liquid flow, which subsequently increases the thickness of the water layer ($\gtrsim 20$ nm). Figure S3 shows the effect of liquid flow on aggregation. In the beginning, the aggregation followed the same fast to slow kinetics described in Figure 1D and S2 (Figure S3A: $t = 0\ \text{s} - 55\ \text{s}$). At $t > 55$ s, we observed a rapid increase in the aggregation speed owing to the spontaneous liquid flow, which pushed the pinned aggregates together, as shown in Figure S3B. The Movie S4 shows the aggregation dynamics that were induced by the liquid flow. The liquid flow between the membranes of the liquid cell induced the fast growth of large aggregates, which increased

their fractal dimensions. In the last image frame (Figure S3A: $t = 70$ s), we clearly see that the large fractal is more compact than the earlier fractals (Figure S3A: $t = 55$ s). This difference occurred because the liquid flow helped de-pin the smaller aggregates and induced their movement, pushing the aggregates together. Using the box-counting method, we calculated the fractal dimension in the last frame to be $D_f \approx 1.63$, which is larger than that of the 2D aggregates of freely diffusing particles ($D_f \approx 1.44$).[12]

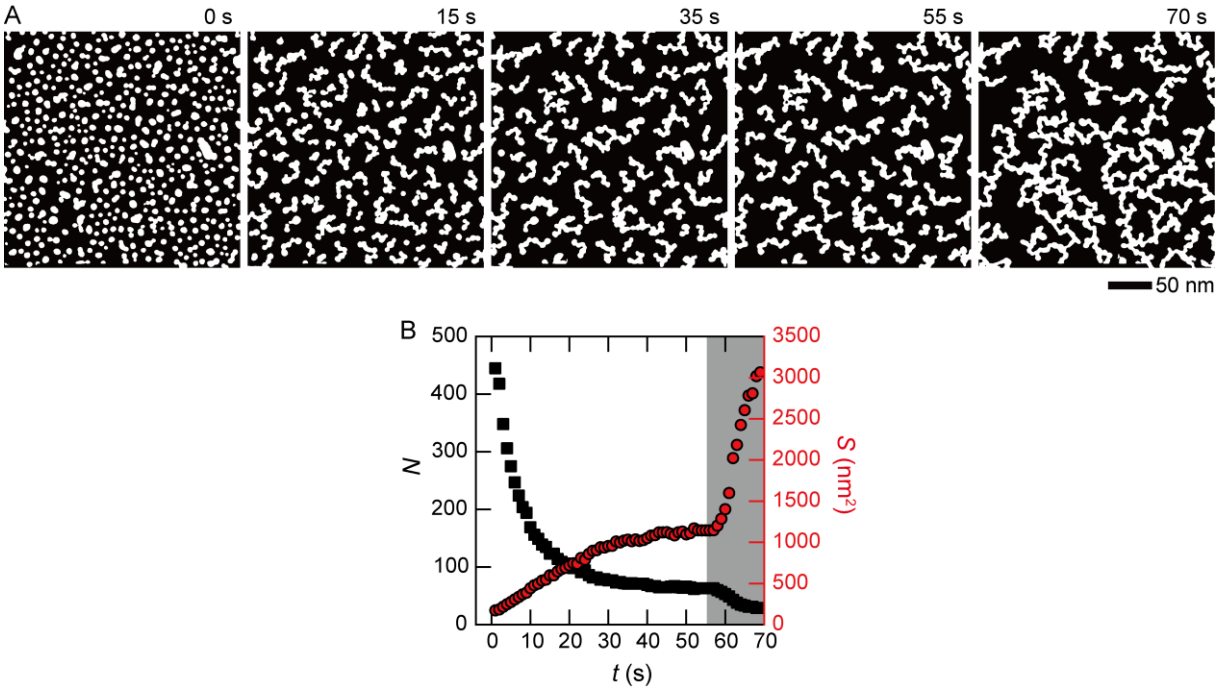

Figure S3. Surface aggregation of the NPs during the liquid flow. (**A**) A sequence of segmented images showing the aggregation during the liquid flow. The first four frames show the aggregation at the solid-liquid interface in a thin water layer, and the last frame shows the liquid flow-induced aggregation when the water flows into the field of view and drags the aggregates. (**B**) Aggregate number (N) and aggregate size (S) versus time, corresponding to the aggregation shown in (A). The grey region corresponds to the flow-induced aggregation.

6. The influence of the electron flux rate

During our experiments, we estimate the electron flux based on the reading of a calibrated CCD camera. We tested the effect of the electron flux on the aggregation kinetics by changing the flux during the experiments, as shown in Figure S4 and Movie S5. At a low flux of $\sim 10\, e^-/(\text{Å}^2 \cdot \text{s})$, the aggregates barely moved, and when the flux was increased to $\sim 90\, e^-/(\text{Å}^2 \cdot \text{s})$, the aggregation process abruptly speeded up. This experiment suggested that a threshold electron flux exists to initiate movement in the physisorbed gold NPs. To establish the electron flux threshold value needed to detach

the gold NPs from the SiN_x surface, we recorded movies with electron fluxes of $\sim 10, 20, 30, 40, 50, 90\ e^-/(Å^2 \cdot s)$. At an electron flux of $\sim 10\ e^-/(Å^2 \cdot s)$, the NPs did not display beam-induced movement (Figure S4: $t < 5$ s)), and at $\sim 20\ e^-/(Å^2 \cdot s)$, the NPs moved very slowly (Movie S6). Therefore, we estimated the electron flux threshold to be $\gtrsim 20\ e^-/(Å^2 \cdot s)$.

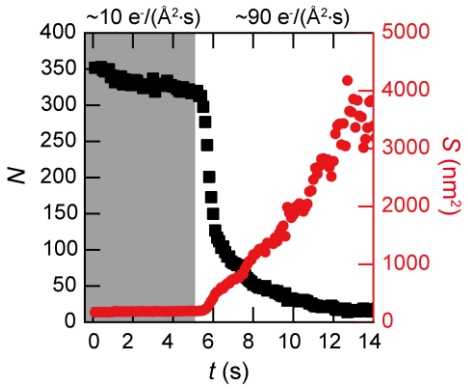

Figure S4. **The effect of the electron flux on the aggregation kinetics of the NPs.** The electron flux was maintained at $\sim 10\ e^-/(Å^2 \cdot s)$ for the first 5 s and was then increased to $\sim 90\ e^-/(Å^2 \cdot s)$.

7. Estimating the jump attempt frequency

A key factor in estimating the energy barrier for the NP detachment is the attempt frequency. We estimated the attempt frequency based on the equipartition theorem for a particle in a square potential well, where each degree of freedom of a particle has an average energy of $^1/_2\, k_B T$.[16]

First, we considered the rotational motion of the NP aggregates. A pinned aggregate will rotate on the surface of SiN_x, so it has only one rotational degree of freedom: $^1/_2\, k_B T = {}^1/_2\, I\omega^2$. Here, I is the aggregate's moment of inertia, and ω is its rotational speed. The moment of inertia (I) can be estimated using the size and shape of the aggregates. The rotational speed allows the NP aggregate to rotate around the pinning point within a potential barrier. We simplified the rotational potential barrier as a square potential well within a rotation range of $\alpha = 10°$ based on our experimental observations. Thus, for an angular speed (ω) and potential well width (α), the attempt frequency is given as $\nu = \omega/\alpha$.

In a similar manner, we estimated the attempt frequency for the translational movement of the aggregates on the surface. A pinned aggregate will attempt to jump out of the pinning site in both the *x* and *y* directions. If we assume that an aggregate has a mass of *M*, then each dimension (*x* and *y*) has a kinetic energy of $^1/_2\, k_B T$ (i.e., $^1/_2\, k_B T = {}^1/_2\, M v_i^2, i = x, y$). The jump attempt frequency for an aggregate for a jump that leads to translation motion, i.e., a jump out of the pinned site in both the *x* and *y* direction, is given by $\nu_i = \omega / L_i$, where L_i is the width of the energy barrier associated with the pinning site. Based on our observed jumps, the width of the pinning site can vary from 2 nm to 20 nm. We estimated the jump attempt frequency (ν) by choosing $L_i = 10$ nm as the typical length scale. Next, using the calculated jump attempt frequency ν and the successful jump rate Γ from our observations, we calculated the pinning strength.

For the aggregate fragments in Figure 3A and Figure 3D, the translational and rotational jump attempt frequencies were $\nu = 2.4 \times 10^6$ Hz and $\nu = 1.4 \times 10^8$ Hz, respectively. The successful jump rate for the translation and rotation were Γ_t = 1/80 (1 successful jumps during 80 s of observation) and Γ_r = 11/40 (11 successful jumps during 40 s). Using equation 2 from the main text, we estimated the potential barrier pinning the translational and rotational movements of these aggregates to be $\sim 19\, k_B T$ and $\sim 20\, k_B T$, respectively.

8. Mechanism of the surface pinning

The interactions between the charged NPs and the SiN_x membrane can be estimated using the Derjaguin-Landau-Verwey-Overbeek (DVLO) theory.[17] In DLVO theory, the net interaction energy, U_{net}, between a gold NP and a flat SiN_x substrate is the sum of an attractive van der Waals (vdW) interaction and a repulsive double-layer (DBL) interaction:

$$U_{\text{net}} = U_{\text{vdW}} + U_{\text{DBL}} = -\frac{AR}{6d} + RZe^{-\kappa D} \quad (5)$$

where A is the Hamaker constant for gold and SiN_x interacting through water ($A \sim 10^{-19}$ J),[18] $R = 10$ nm is the radius of the gold NPs, and *d* is the separation between the interacting surfaces (gold to SiN_x). κ is the inverse Debye screening length in the solution, and Z is the DBL interaction constant. Both κ and Z change during the electron beam irradiation because the NPs and membrane become charged and radiolytic species are produced:[17]

$$\frac{1}{\kappa} = \frac{0.304\times10^{-9}}{\sqrt{M}} \quad (6)$$

$$Z = 9.22 \times 10^{-11} \times \tanh(\frac{\psi}{103})^2 \quad (7)$$

where M is the molar ionic strength of the solution, and ψ is the surface potential of the interacting surfaces in mV. Under an electron flux of $\sim 20\ e^-/(\text{Å}^2 \cdot \text{s})$, both M and ψ change due to radiolysis.

When the sample is irradiated by an electron beam, two major effects will occur, which influence both M and ψ. The first effect is that, under the electron beam, both the SiN_x membrane and gold NPs acquire a positive charge,[14, 19] resulting in an increase in the surface potential (ψ) for the interacting surfaces of the NPs and the membrane. The second effect is the beam-induced radiolysis of water, which increases the effective ionic strength of the solution. Schneider N. *et al.* estimated that the ionic strength of neat water (10^{-7} M) can reach a steady state of 10^{-6} M within milliseconds.[20] We estimated that the surface potential can reach up to 100 mV as a result of the beam-induced charging.[15] According to our estimates, during the TEM imaging, the effect of the surface potential change has a greater influence on the DBL interaction than the change in the solution's ionic strength. Unlike the DBL force, the vdW force is largely insensitive to variations in the electrolyte concentration and pH. Further, at small distances, the value of the attractive vdW force always exceeds the repulsive DBL force. We plotted the net interaction energy for different ψ as a gradual charging process, as shown in Figure S5.

Prior to electron beam imaging, the NPs were physisorbed onto the membrane by the strong vdW attraction between the NPs and the membrane. As the membrane's surface charges and its potential increases during the electron beam irradiation, the increase in the repulsive DBL force shifts the DLVO energy curve upward (Figure S5). When ψ is sufficiently large ($\psi > 50$ mV), the net DLVO interaction energy reaches zero at $D \sim 7$ Å. Note that the vdW force is still greater than the DBL force when a NP is very close to the surface. However, the attractive vdW force can be overcome by thermal fluctuations, which allows detachment of the NPs. This qualitative description agrees with other earlier reports that describe NP dynamics on a SiN_x membrane in a liquid cell during e-beam irradiation.[14, 19, 21, 22]

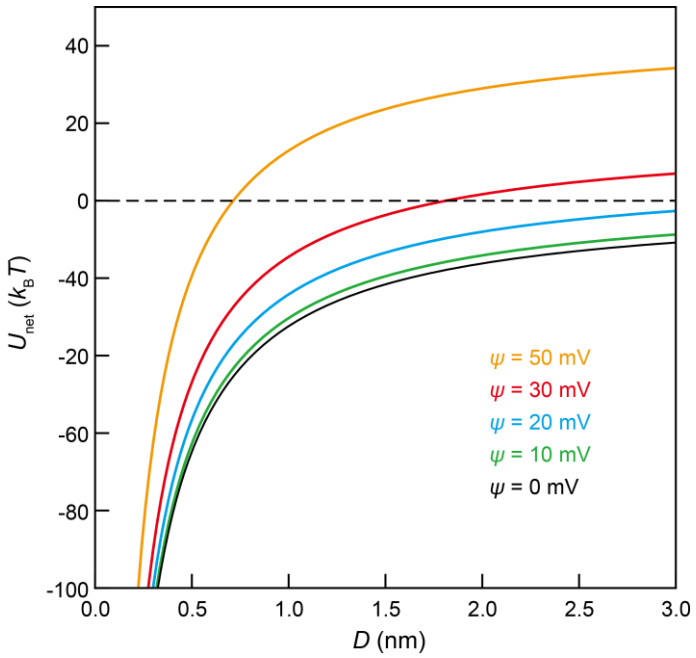

Figure S5. DLVO interaction energy between a spherical gold NP and a flat SiN_x membrane. During the electron beam-induced charging, the membrane surface potential increases, and the NP shifts the net DLVO interaction upward, reducing the height of the energy barrier needed to detach a NP from the membrane surface. The curves display the net interaction at different surface potentials at an ionic strength of water of 10^{-6} M.

In our experiments, the NPs were confined to the solid-liquid (SiN_x-water) interface by a thin (<20 nm) water film on a membrane, and the diffusion of these confined NPs was suppressed.[13, 21, 23] The DLVO interaction between the NPs and the smooth surfaces alone cannot explain the transient pinning of the NPs and their aggregates during the aggregate growth because our observations reveal that the duration and strength of the pinning vary across the NPs (Figure 2). The surface of the SiN_x membrane is not atomically flat (Figure S6) and can modify the vdW attraction to promote the pinning of the NPs by the membrane.[15] Additionally, SiN_x is known to hydrolyse in water, and the membrane may have regions with a nonuniform charge distribution containing silanols (Si-OH) and silazanes (Si_2-NH, Si-NH_2).[24] These randomly distributed charge groups can modify the DBL force, increasing the attraction between the NPs and certain spots on the membrane (Figure S6).

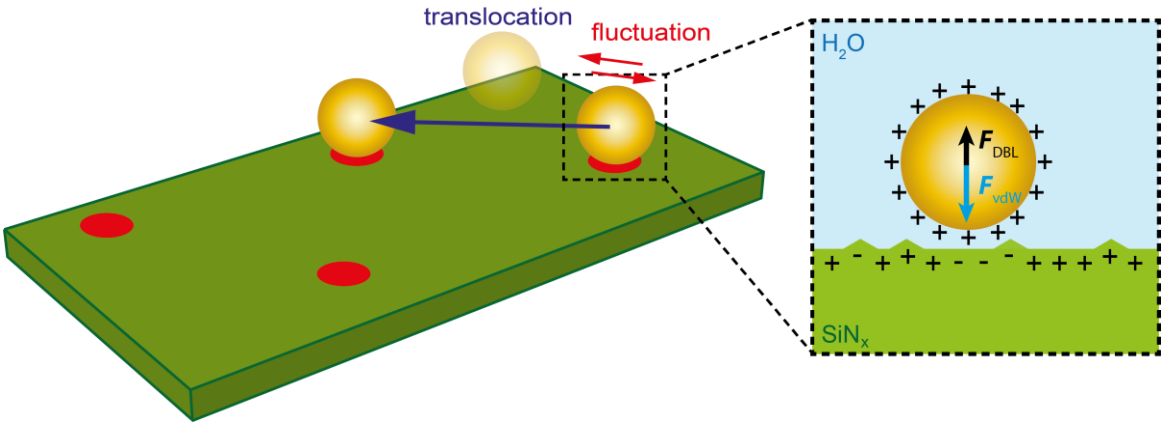

Figure S6. Schematic illustration of in-plane NP dynamics and pinning. The red spots on the membrane surface represent the randomly distributed pinning sites. The enlarged image illustrates the microscopic picture of a pinning site. Thermal excitation can cause the NP to move in any direction and is the main driving force for in-plane movements.

9. Supporting movie captions

Movie S1: A movie of the aggregation process shown in Figure 1 and 2. This movie shows a typical aggregation process within a thin water layer recorded for 119.4 s. The value of the electron flux used for imaging was $\sim 40\ e^{-}/(\text{Å}^2 \cdot \text{s})$.

Movie S2: A movie showing the template matching results of the segmented binary image frames corresponding to Figure 3A. The rectangular box shows the best fit for the aggregate. The images are cropped to feature the selected aggregate.

Movie S3: A movie showing the template matching results of the segmented binary image frames of the aggregates corresponding to Figure 3D. The rectangular box shows the best fit for the aggregate. The images are cropped to feature the selected aggregate.

Movie S4: A movie showing the aggregation process of the NPs that corresponds to Figure S3. This movie shows the transition from fast to slow aggregation with the increasing aggregate size. At the end of the movie, a thick water layer flows into the field of view and drags the large aggregates. The kinetics in Figure S3B shows an increased aggregation rate due to the water flow at $t > 56$ s. The value of the electron flux used for the imaging was $\sim 40\ e^{-}/(\text{Å}^2 \cdot \text{s})$.

Movie S5: A movie showing the aggregation process of the NPs that corresponds to Figure S4, which reveals the effect of the electron flux. The electron flux was maintained at $\sim 10\ e^{-}/(\text{Å}^2 \cdot \text{s})$ during the initial 5 s, but then, it was abruptly increased to $\sim 90\ e^{-}/(\text{Å}^2 \cdot \text{s})$. The gold NPs do not move under the low electron flux ($\sim 10\ e^{-}/(\text{Å}^2 \cdot \text{s})$), and fast NP movement was observed at the high electron flux ($\sim 90\ e^{-}/(\text{Å}^2 \cdot \text{s})$).

Movie S6: A movie showing the aggregation process of the NPs acquired at an electron flux of $\sim 20\ e^{-}/(\text{Å}^2 \cdot \text{s})$. By comparing Movie S5 and S6, we established that the threshold electron flux needed for NP movement was $\gtrsim 20\ e^{-}/(\text{Å}^2 \cdot \text{s})$.

10. Supporting references

1. K. J. Millman and M. Aivazis, *Comput. Sci. Eng.*, 2011, **13**, 9-12.
2. S. Van Der Walt, S. C. Colbert and G. Varoquaux, *Comput. Sci. Eng.*, 2011, **13**, 22-30.
3. T. E. Oliphant, *Comput. Sci. Eng.*, 2007, **9**, 10-20.
4. G. Bradski, *Doctor Dobbs Journal*, 2000, **25**, 120-126.
5. S. van der Walt, J. L. Schonberger, J. Nunez-Iglesias, F. Boulogne, J. D. Warner, N. Yager, E. Gouillart and T. Yu, *PeerJ*, 2014, **2**, e453.
6. S. Behnel, R. Bradshaw, C. Citro, L. Dalcin, D. S. Seljebotn and K. Smith, *Comput. Sci. Eng.*, 2011, **13**, 31-39.
7. L. P. Coelho, *J. Op. Res. Softw.*, 2013, **1**, e3.
8. J. D. Hunter, *Comput. Sci. Eng.*, 2007, **9**, 90-95.
9. N. Sarkar and B. B. Chaudhuri, *IEEE Transactions on Systems, Man, and Cybernetics*, 1994, **24**, 115-120.
10. C. D. McGillem and M. Svedlow, *IEEE Transactions on Geoscience Electronics*, 1976, **14**, 44-49.
11. A. Y. Kim and J. C. Berg, *Langmuir*, 2000, **16**, 2101-2104.
12. P. Meakin, *Phys. Scr.*, 1992, **46**, 295.
13. J. Lu, Z. Aabdin, N. D. Loh, D. Bhattacharya and U. Mirsaidov, *Nano Lett.*, 2014, **14**, 2111-2115.
14. S. W. Chee, Z. Baraissov, N. D. Loh, P. T. Matsudaira and U. Mirsaidov, *J. Phys. Chem. C*, 2016, **120**, 20462-20470.
15. U. Mirsaidov, H. Zheng, D. Bhattacharya, Y. Casana and P. Matsudaira, *Proc. Natl. Acad. Sci.*, 2012, **109**, 7187-7190.
16. W. Greiner, D. Rischke, L. Neise and H. Stöcker, *Thermodynamics and Statistical Mechanics*, Springer New York2000.
17. J. N. Israelachvili, in *Intermolecular and Surface Forces (Third Edition)*, Academic Press, San Diego2011, pp. 291-340.
18. J. N. Israelachvili, in *Intermolecular and Surface Forces (Third Edition)*, Academic Press, San Diego2011, pp. 253-289.
19. E. R. White, M. Mecklenburg, B. Shevitski, S. B. Singer and B. C. Regan, *Langmuir*, 2012, **28**, 3695-3698.
20. N. M. Schneider, M. M. Norton, B. J. Mendel, J. M. Grogan, F. M. Ross and H. H. Bau, *J. Phys. Chem. C*, 2014, **118**, 22373-22382.
21. A. Verch, M. Pfaff and N. de Jonge, *Langmuir*, 2015, **31**, 6956-6964.
22. T. J. Woehl and T. Prozorov, *J. Phys. Chem. C*, 2015, **119**, 21261-21269.
23. Y. Liu, X.-M. Lin, Y. Sun and T. Rajh, *J. Am. Chem. Soc.*, 2013, **135**, 3764-3767.
24. V. V. Tsukruk and V. N. Bliznyuk, *Langmuir*, 1998, **14**, 446-455.